JOURNAL OF AIRCRAFT
Vol. 45, No. 3, May–June 2008

Reactive Flow Control of Delta-Wing Vortex

Yong Liu,* Ming Wu,† J. Jim Zhu,‡ and Douglas A. Lawrence§
Ohio University, Athens, Ohio 45701
Ephraim J. Gutmark¶
University of Cincinnati, Cincinnati, Ohio 45221
James H. Myatt**
U.S. Air Force Research Laboratory (AFRL/VACA), Wright–Patterson Air Force Base, Ohio 45433
and
Cameron A. May††
University of Cincinnati, Cincinnati, Ohio 45221

DOI: 10.2514/1.28449

In this paper, the reactive flow control of delta-wing leading-edge vortices using along-core pulse-width-modulation flow injection is presented. Leading-edge vortices on the upper surface of a delta wing can augment lift. Manipulating breakdown points of leading-edge vortices can effectively change the delta wing's lift and drag and generate attitude-control torque. In this paper, a black-box dynamic model for active flow control of vortex breakdown points is identified from wind-tunnel data using a model scheduling method. Based on the identified model, a closed-loop active flow controller is developed. Simulation and real-time wind-tunnel test show that the closed-loop controller can effectively manipulate the upper surface pressure of the delta wing, which indicates that the closed-loop controller can effectively control vortex breakdown points.

Nomenclature

A_{jet}	=	jet orifice area. (in.^{2})
C_P	=	pressure coefficient
C_μ	=	jet momentum coefficient
e_u	=	feedback control input
e_x	=	error state
e_y	=	output error
K_i	=	integral feedback gain
K_o	=	observer feedback gain
K_p	=	proportional feedback gain
P	=	dynamic pressure
P_∞	=	freestream pressure
S	=	delta-wing area (in.^{2})
U_∞	=	freestream wind velocity (in./s)
u	=	duty cycle input
$\bar{u}$	=	nominal control input
u_δ	=	broadband component of duty cycle input
u^o	=	static duty cycle
V_{jet}	=	flow speed at jet orifice (in./s)
y	=	dynamic pressure sensor output (V)
y_{com}	=	dynamic pressure command (V)
y_δ	=	deviation component of dynamic pressure sensor output (V)
y^o	=	steady dynamic pressure sensor output (V)
α	=	scheduling variable
ζ	=	augmented output error
$\hat{\zeta}$	=	observer output
$\tilde{\zeta}$	=	observer output error
η	=	augmented error states
$\hat{\eta}$	=	observer state
$\tilde{\eta}$	=	observer state error
ρ	=	air density

Presented as Paper 6189 at the AIAA Guidance, Navigation, and Control Conference and Exhibit, Keystone Colorado, 21–24 August 2006; received 23 October 2006; revision received 21 September 2007; accepted for publication 21 September 2007.

*Ph.D. Candidate, School of Electrical Engineering and Computer Science; currently Control System Engineer, Cardinal Health, Incorporated; Yong.Liu.1@ohio.edu. Member AIAA.
†Graduate Student, School of Electrical Engineering and Computer Science.
‡Professor, School of Electrical Engineering and Computer Science; zhuj@ohio.edu. Senior Member AIAA.
§Associate Professor, School of Electrical Engineering and Computer Science; dal@ohio.edu.
¶Professor, Aerospace Engineering and Engineering Mechanics; Ephraim.Gutmark@uc.edu.
**Senior Aerospace Engineer, Air Vehicles Directorate. Senior Member AIAA.
††Graduate Student, Aerospace Engineering and Engineering Mechanics.

I. Introduction

THE delta wing has been in the second half of the twentieth century a common platform for modern high-speed civil and military aircraft due to low drag in supersonic flight as a result of the swept leading edge of the wing and high lift in subsonic flight at moderate angles of attack due to the formation of vortices over the upper surface. At moderate to high angles of attack, there exist large leading-edge vortices propagating on the top surface of the delta wing. These vortices can effectively augment the total lift. However, during higher angle-of-attack flight, a phenomenon known as vortex breakdown (VBD) may occur, which plays a role in limiting the performance of the aircraft. Onset of vortex breakdown is observed as the vortex diameter increases, the axial velocity of the vortex core decreases, and the circumferential velocity decreases. Aft of the vortex breakdown location, flow becomes turbulent, which results in a rapid loss of lift. Thus, controlling vortex breakdown locations on delta wings is desirable for extending the performance envelope of delta-wing aircraft.

A substantial amount of research has been dedicated to the control of aerodynamic flows using both passive and active control mechanisms. Passive vortex control devices, such as vortex generators and winglets, are attached to the wing and require no energy input. Passive vortex control devices are designed to perform optimally over a small range of flight conditions. Active vortex

control systems require energy input and can operate effectively and efficiently over a wider range of flight conditions. In the past few decades, many researchers have studied the leading-edge vortices of highly swept wings, and several different techniques have been developed in an attempt to delay breakdown. In [1], a historical review of vortex breakdown active-flow control is provided. Vortex breakdown active flow-control techniques can be categorized into two main classes: mechanical methods and pneumatic methods. Examples of mechanical vortex breakdown control techniques are variable-sweep delta wings [2] and microelectromechanical devices mounted on the surface of the wing. The mechanical vortex breakdown control methods change the geometry of the wing for different flow conditions. Some pneumatic methods include span-wise blowing [3–5], tangential leading-edge blowing [6], leading-edge suction [7], trailing-edge blowing [8–10], and along-core blowing [11–15]. Other active flow-control methods, such as synthetic jet control on delta-wing leading edges, is also effective for changing the aerodynamic characteristics of delta wings [16–18].

Along-core blowing incorporates a jet of air directed down the core of the vortex. The objective of this technique is to supply the momentum necessary to overcome the adverse pressure gradient, maintain high axial velocities in the core, and delay vortex breakdown. In [11], the authors observed that the vortex breakdown is pushed downstream almost the instant the jet is turned on, which gives rise to the potential of using a pulsed jet for improved efficiency. In [14], the author observed that the effectiveness of the flow control improved as the blowing-mass flow rate was increased. Additional studies in along-core blowing have attempted to control the vortices produced by the slender forebodies of aircraft at high angles of attack for the purposes of roll and yaw control [19].

Gutmark and Guillot [15] proposed controlling the breakdown of delta-wing leading-edge vortices by injection of a small control jet into or near the vortex core. Experiments were conducted on a 60-deg half-delta wing in a wind tunnel with a Reynolds number of 260,000 based on the freestream conditions and the wing's root chord. Optimization of the control jet parameters was performed to maximize the control authority gained by varying the locations and orientations of the jet and by using different blowing coefficients. The optimal jet pitch and azimuthal angles varied with the jet location [15,20]. The optimal orientation of the jet ensured that the momentum carried by this jet was injected directly into the core of the vortex, thus accelerating the air along the centerline of the vortex and delaying vortex breakdown. The jet momentum was also optimized between two limits: too much injection would cause the jet to pass through the vortex without being entrained into it, whereas too little injection would not provide enough momentum to the vortex to maintain its coherence. Although, the optimal injection conditions varied somewhat with the angle-of-attack, along-core injection was shown to be an effective technique for manipulating vortex breakdown location in a wide range of angles of attack [15].

Wind-tunnel experiments were used to study different flow-control actuation methods for vortex breakdown location with along-core injection. Static pressure taps on the upper surface were used to determine vortex breakdown location. It was observed that pulse-width-modulation (PWM) flow injection with fixed flow pressure and continuous injection with varying injection momentum are equally effective for controlling vortex breakdown. For the PWM injection, the optimized configuration of nozzle azimuth and pitch angles, injection momentum, PWM frequency, and duty cycles to delay the vortex breakdown were analyzed using wind-tunnel data [20]. The optimal jet configuration was the azimuth angle at 170 deg, pitch angle at 35 deg, momentum coefficient at 0.023, normalized modulation frequency $F_N = 1.08$ based on the freestream velocity and wing's root chord ($F_N = fCr/U_\infty$), duty cycle at 50%, and momentum coefficient at 0.023, at which the nondimensional momentum coefficient is defined as

$$C_\mu = \frac{A_{\text{jet}}}{S}\left(\frac{V_{\text{jet}}}{U_\infty}\right)^2$$

In most research on active flow control of delta-wing vortex breakdown, the active flow control is introduced in an open-loop fashion in which the effects of the proposed methods are shown under different configurations. For practical applications, the open-loop strategy depends on the availability of accurate and comprehensive experimental study. It is extremely difficult to accurately model the changes in the system dynamics due to varied operating conditions, inevitable external disturbances, and measurement noise. To achieve the preferred aerodynamic performance, a closed-loop active, hereafter called reactive, flow-control method is desired to compensate for uncertainty of the active flow-control system and to reject disturbances. One challenge of a closed-loop active flow-control is to identify a simplified dynamic model, which represents the essential dynamics of the flowfield and also is suitable for controller design because underlying active-flow mechanisms are usually very complicated and highly nonlinear. A popular modeling method in active flow control is proper orthogonal decomposition (POD) [21–29]. Another challenge of closed-loop active flow control is to design a robust, nonlinear controller based on the identified nonlinear model. Many advanced nonlinear control methods depend on an accurate plant dynamic model, which is usually unavailable or inaccurate.

In [30], a successful implementation of a closed-loop feedback control of vortex breakdown is presented. It is demonstrated on a variable sweep delta wing. The pressure fluctuation of an unsteady pressure sensor near the trailing edge is used to indicate the vortex breakdown position. The dynamic response of the closed-loop active flow-control system in [30] is represented by a first-order system.

In this paper, the reactive flow control of vortex breakdown with along-core injections is presented. The focus is on the development of a control-oriented flowfield dynamics model and the closed-loop controller design and wind-tunnel testing. Different from [30], in the presented flow-control system, the pressure measured with an unsteady pressure sensor on the upper surface of the delta wing is used to indicate the vortex breakdown position. The duty cycle of the PWM injection is used as the control actuation variable. Based on the experimental results in [20], first a nonlinear system identification approach is employed to obtain a simplified flowfield dynamics model for feedback controller design. Wind-tunnel experiments for identifying the vortex breakdown process model are designed and conducted. A nonlinear dynamic system model is identified from the wind-tunnel experiment results. Then, a trajectory linearization-type nonlinear controller is designed based on the identified dynamic model. The closed-loop vortex breakdown active flow-control system is simulated and real-time tested in wind-tunnel experiments. In the wind-tunnel real-time test, the reactive flow control of vortex breakdown is able to manipulate the upper surface pressure of the delta wing, even with perturbations.

In Sec. I, the experiment equipment and the data acquisition and real-time control system are introduced. In Sec. II, the nonlinear dynamic modeling development for delta-wing active vortex control is presented. In Sec. III, a trajectory linearization type gain-scheduling controller based on the identified nonlinear model is developed. Simulation and real-time test results of reactive vortex control are presented in Sec. IV.

II. Wind-Tunnel Experiment, Data Acquisition, and Real-Time Control System

Wind-tunnel experiments for delta-wing vortex control were conducted in the low-speed wind tunnel in the University of Cincinnati Aerospace Engineering Department's Fluid Mechanics and Propulsion Laboratory. The wind tunnel is a subsonic closed-circuit wind tunnel manufactured by Engineering Laboratory Design, Inc., located in Lake City, Minnesota. The test section has a cross section of 2 ft × 2 ft and is 8 ft in length. The wind tunnel is rated by the manufacturer to speeds of up to 300 ft/s and also is equipped with a heat exchanger and a West model 3800 temperature controller so that the internal temperature can be maintained at a desired setting.

Table 1 Dimensions of delta wing

Sweep angle	60 deg
Leading-edge bevel angle	30 deg
Span	0.394 m
Root chord	0.343 m
Angle of attack	15 deg
Freestream velocity	20 m/s

The delta-wing model used in the experiment was an aluminum 60-deg sweep delta wing with a 30-deg leading-edge bevel on the lower surface. The dimensions of the test delta wing are shown in Table 1. Blockage effects were less that 5% at the angle of attack used. This is below the level that requires corrections to measurements. The wind tunnel's wall boundary layer thickness at the wing location was about 2 cm, and the wind-tunnel velocity profile outside the boundary layer was flat. The distance from the wing trailing edges to the outer edge of the boundary layer ranged from 9 to 28 cm, such that the wall effects on the vortex behavior were minimal. A top plate for the wing was designed with 96 static pressure taps on the surface in four span-wise rows located at 35, 55, 75, and 95% of the root chord, as shown in Fig. 1. A second top plate was fabricated to accommodate dynamic pressure transducers. The dynamic pressure instrument was a piezoelectric transducer manufactured by Endevco, Inc., with a pressure range of 0–2 psia. The flow injection valve is an orifice poppet valve from Parker Valves, Inc., driven by a 24 VDC signal from an Iota-1 controller also manufactured by Parker Valves, Inc. Figure 2 shows the delta-wing model mounted in the wind tunnel.

In the data acquisition and real-time control experiments, two different instrumentation systems were used. The first hardware used was a LabVIEW system from National Instruments. It was used in static and dynamic pressure data acquisition. The LabVIEW system

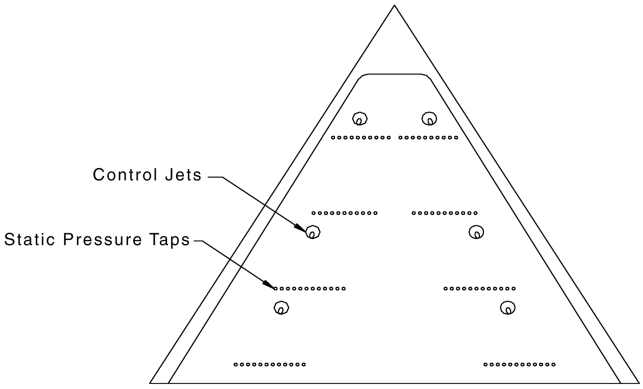

Fig. 1 Delta-wing control jets and static pressure sensor.

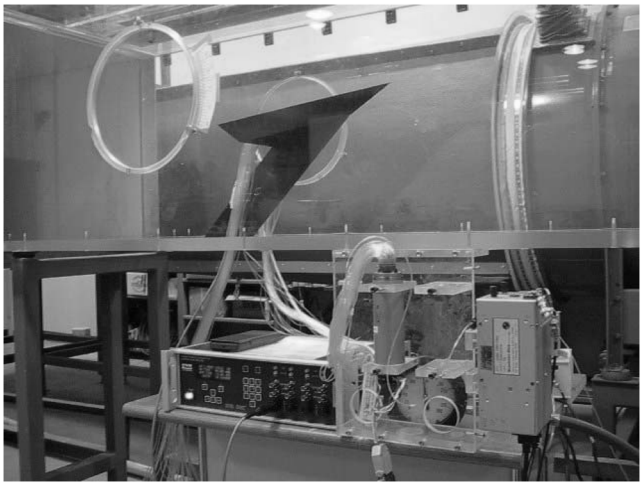

Fig. 2 Wind-tunnel test section for delta-wing flow control.

was capable of generating PWM signals to drive the control jets and to measure the pressure sensor signals. The highest sampling rate of the LabVIEW system used in the experiments was 4 kHz. However, the LabVIEW system did not support real-time tasks, and so it could not be used for real-time closed-loop control. The second hardware used was a Wincon/RTX system from Quanser. Wincon/RTX is a rapid-prototyping system for control system applications. RTX provides a real-time extension of the Windows OS. The Wincon toolbox, used with Simulink and Real-Time Workshop from The MathWorks, could generate real-time executable code directly from the Simulink model. In this project, Wincon 3.2, RTX 5.1, and a multi-Q PCI board were used in dynamic tests for system identification and real-time control tests. The highest sampling rate that can be achieved using the Wincon system is 2 kHz.

Because it has been shown that both a continuous jet and pulsed jet can effectively control the jet momentum, an on–off valve control actuator was chosen over a continuous actuator for lower cost and better efficiency. But this limited the choices of control actuation variable to either pulse-width modulation or on–off frequency modulation (FM). The FM works at the limit of the valve's bandwidth, which is sensitive to the valve's working conditions, such as lubrication, whereas PWM works within the designed bandwidth of the valve, which is more robust.

A PWM duty-cycle quantization resolution problem was identified in the experiments. In the LabVIEW configuration, the highest sampling rate was 4 kHz, and the desired PWM frequency was 55 Hz. Therefore, only 72 ($4000/55 = 72.72$) discrete pulse-width values could be generated over the 0–100% duty-cycle range. In the WinCon/RTX configuration, the pulse-width resolution was even lower, only 36 values, because the highest sampling rate was only 2 kHz. The low duty-cycle resolution would create an unacceptable level of quantization noise for closed-loop control actuation, and for the proposed system identification approach, which uses a small-variance white noise at a set of nominal duty-cycle values to excite the flowfield dynamics. To increase the resolution of the duty-cycle control variable, a Microchip PIC18F458 microcontroller, a high-end 8-bit microcontroller with highest clock rate 40 MHz, was used to generate the PWM signal at 55 Hz with 10-bit (1024) resolution. When using the PIC18F458 as a high-resolution PWM generator, the PWM signal was no longer generated by LabVIEW or WinCon directly. Instead, an analog signal ranging between 0 to 5 V, which represented 0–100% pulse width, was sent to the PIC18F458. The PIC18F458 picked up the command via a 10-bit built-in A/D converter, and used a 4-MHz crystal to trigger the PWM signal. Thus, the PWM signal resolution was independent of the sampling rates of the LabVIEW and WinCon systems.

III. Nonlinear Model Development for Vortex Active Flow Control

The average location of the vortex breakdown was determined from the static pressure distribution over the wing in the wind-tunnel tests [15,20]. Surface dynamic pressure fluctuations can be detected near the VBD average locations due to the VBD movement upstream and downstream of the average location [31]. Consequently, a dynamic pressure sensor was installed at 66.7% root chord (11.43 cm from trailing edge) and at 6.35 cm span from root chord for feedback control. This sensor was under the vortex core on the delta-wing upper surface, and was close to the vortex breakdown location without jet injection. When the vortex breakdown was delayed, the dynamic pressure at this position would decrease. The pressure signal is represented by the pressure coefficient C_p, which is defined as

$$C_p = (P - P_\infty)/\left(\tfrac{1}{2}\rho_\infty U_\infty^2\right)$$

The vortex breakdown was indicated by the increase of C_p. The unsteady pressure sensor calibration constant was 0.070391 (mV/psi). The sensor output was amplified 1000 times and then sampled by data acquisition board. The dynamic pressure

at 20 m/s wind speed test was 0.0462 psi. The calibrated unsteady pressure coefficient was calculated as

$$C_p = \frac{y}{1000 \times 0.070391 \times 0.0462} = 0.3075y$$

where y is the amplified pressure sensor output voltage. When the vortex breakdown was delayed, the pressure sensor output voltage increases. From the viewpoint of control system design, the system input is the duty cycle of the PWM injection, and the system output is the amplified pressure sensor output voltage.

A nonlinear dynamic model was identified from experimental data with the PWM duty cycle as system input, and amplified pressure sensor voltage as system output. Numerous methods for empirically based model development have been applied to fluid dynamics problems. Proper Orthogonal Decomposition seeks to identify from a collection of flowfield snapshots a set of optimal modes (with respect to an energy capture criterion) such that the Galerkin projection of the Navier–Stokes onto the span of these modes yields a reduced-order control-oriented model [21–29]. Given that the flowfield snapshots were not available for this work, POD could not be employed.

Other methods for modeling unsteady aerodynamic phenomena use a parametric model, often based on physical insight, in which the free parameters are tuned using experimental data obtained from available sensor measurements [32–35]. Rather than impose a fixed model structure, the approach adopted in this work employs a black-box approach in which system identification methods are used to determine model order as well as model parameter values. Techniques for linear system identification [36–38] are more widely available than for the nonlinear case [39]; however, linear models can only predict the behavior of a nonlinear system in a vicinity of an equilibrium point or other nominal condition.

To exploit the maturity of linear system identification techniques while overcoming the inherent limitation of linear models, we employ an approach for nonlinear system identification motivated by gain-scheduled control system design [40], which we refer to as model scheduling. This approach was developed explicitly for the purposes of experimental modeling the unsteady aerodynamic loading on a delta wing operating at high angle of attack [41]. The basic idea is to identify a set of linear models about a collection of equilibria from which a nonlinear model is constructed that instantaneously schedules the linear models based on the input signals and/or other internal variables. The overall procedure consists of the following four steps:

1) Conduct static tests on the system to acquire equilibrium data characterizing constant input signal values and associated constant steady-state output values. Characterize the output values as a function of the input values.

2) For a discrete set of equilibria, perform linear system identification to obtain a set of linear state-space models that describe the system's small-signal behavior in a vicinity of each of the equilibria.

3) Interpolate or curve fit the parameters in the state-space models to yield a smoothly parameterized family of linear models.

4) Construct a nonlinear model that satisfies static and dynamic linearization requirements with respect to the parameterized family of linear models.

A. Static Test

The control jet was pulse-width modulated at normalized modulation frequency of 1.08 based on the freestream velocity and wing's root chord, with a duty cycle that was programmable between 0% and 100% in $1/1024 \approx 0.1\%$ increments. For the static tests, 11 constant pulse widths ranging from 0 to 100% in 10% increments were applied to the PWM control jet input. For each fixed pulse width, three 10-s trials were performed. The raw pressure sensor voltage output was analog filtered for antialiasing at a cutoff frequency of 100 Hz and then sampled at a 2000-Hz rate. The first 3 s of data that include the unwanted transient response were discarded. The final seven seconds of data therefore comprised the steady-state response of the dynamic pressure sensor to the constant duty-cycle value.

For each duty-cycle value, the sensor voltage time histories were averaged across the three trials and then time averaged over the final seven seconds to yield the static steady-state value of the pressure sensor voltage for the corresponding duty-cycle value. These data points with linear interpolation are plotted in Fig. 3, along with error bars indicating the variance associated with the time averaging. Also plotted are the steady-state output voltages of the static pressure sensor derived from an earlier experiment that used the original low-resolution LabVIEW data collection system. It can be seen that the high-resolution PWM generator, along with the correction of an earlier problem with the unsteady pressure sensor, greatly reduced the variance in the static test data.

It is observed from Fig. 3 that the PWM control actuator appears to be saturated for duty cycles greater than 40%, as the gain drops sharply from approximately 0.2 volts per 10% duty cycle to about 0.025 volts per 10% duty cycle. This drastic change in control effectiveness of the actuator is to be accommodated by the closed-loop controller, and its effects can be seen from the closed-loop control test results presented in the sequel.

B. Dynamic Test

The static test curve is used to determine the equilibria about which to conduct dynamic tests as follows. The static curve is first divided into regions, which are well approximated by a linear curve. The midpoint of each region then determines the static duty-cycle value to which a broadband (random noise) perturbation is added. The width of each region then determines the amplitude of the broadband component of the duty-cycle input signal. Dynamic tests were conducted on each region for broadband components with amplitude equal to 25, 50, and 75% of the region width. The dynamic test parameters are summarized in Table 2.

The composite duty-cycle input signal is denoted $u(t) = u^o + u_\delta(t)$, where u^o is the static duty-cycle component given by the region's midpoint, and u_δ denotes the broadband component. The resulting pressure sensor response denoted $y(t)$ is decomposed as $y(t) = y^o + y_\delta(t)$ in which y^o is the static response value corresponding to u^o as determined from the static curve, and the deviation component is given by $y_\delta(t) = y(t) - y^o$. Figure 4 contains the time histories of the pressure-sensor response and control jet duty-cycle input signal for region 1 for perturbation amplitudes scaled to 75% of the region width.

For each region, the deviation components of both input and output signals were sampled at 2000 Hz, and linear system identification algorithms were applied to the discretized signals to yield a fifth-order discrete-time linear-state-space model. Two methods, eigensystem realization [36] and subspace identification

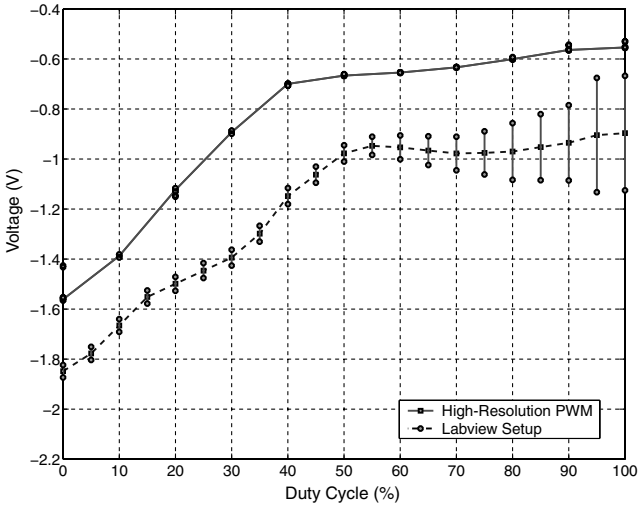

Fig. 3 Steady-state pressure sensor voltage vs jet duty cycle.

Table 2 Dynamic test parameters

	Range	Width	Nominal duty cycle	Noise amp 25% width	Noise amp 50% width	Noise amp 75% width
Region1	0–14.2	14.2	7.10	3.6	7.1	10.7
Region2	14.2–39.6	25.4	26.90	6.3	12.7	19.0
Region3	39.6–52.6	13.0	45.60	3.2	6.5	9.6
Region4	52.6–62.8	10.2	57.70	2.5	5.1	7.5
Region5	62.8–76.6	13.8	69.70	3.4	6.9	10.3
Region6	76.6–100	23.4	87.80	5.8	11.7	17.5

[37], were employed, yielding similar models. The discrete-time models were converted to a continuous-time model via the bilinear transformation [42].

The continuous-time state-space models for each region, indexed by the scheduling variable $\alpha_i = u_i^o$, $i = 1, \ldots, 6$ were cast in modal form specified by coefficient matrices:

$$A(\alpha_i) = \begin{bmatrix} a_{11}(\alpha_i) & -a_{21}(\alpha_i) & 0 & 0 & 0 \\ a_{21}(\alpha_i) & a_{11}(\alpha_i) & 0 & 0 & 0 \\ 0 & 0 & a_{33}(\alpha_i) & -a_{43}(\alpha_i) & 0 \\ 0 & 0 & a_{43}(\alpha_i) & a_{33}(\alpha_i) & 0 \\ 0 & 0 & 0 & 0 & a_{55}(\alpha_i) \end{bmatrix},$$

$$B(\alpha_i) = \begin{bmatrix} 0 \\ 1 \\ 0 \\ 1 \\ 1 \end{bmatrix},$$

$$C(\alpha_i) = [\, c_1(\alpha_i) \quad c_2(\alpha_i) \quad c_3(\alpha_i) \quad c_4(\alpha_i) \quad c_5(\alpha_i) \,],$$

$$D(\alpha_i) = 0$$

Model parameter values are listed in Table 3. This form directly displays the model's eigenvalues or poles as follows:

$$\lambda_{1,2}(\alpha_i) = a_{11}(\alpha_i) \pm j a_{21}(\alpha_i), \qquad \lambda_{3,4}(\alpha_i) = a_{33}(\alpha_i) \pm j a_{43}(\alpha_i),$$

$$\lambda_5(\alpha_i) = a_{55}(\alpha_i)$$

and the c_is are related to the real and imaginary parts of the residues associated with these eigenvalues in a partial fraction expansion of the model's transfer function.

C. Parameter Interpolation

This step simply involves linear interpolation of the state-space-model parameters for each region to yield state-space coefficient matrices that are now functions of the scheduling variable α (representing the PWM duty cycle in the continuous 0–100% range):

$$A(\alpha) = \begin{bmatrix} a_{11}(\alpha) & -a_{21}(\alpha) & 0 & 0 & 0 \\ a_{21}(\alpha) & a_{11}(\alpha) & 0 & 0 & 0 \\ 0 & 0 & a_{33}(\alpha) & -a_{43}(\alpha) & 0 \\ 0 & 0 & a_{43}(\alpha) & a_{33}(\alpha) & 0 \\ 0 & 0 & 0 & 0 & a_{55}(\alpha) \end{bmatrix},$$

$$B(\alpha) = \begin{bmatrix} 0 \\ 1 \\ 0 \\ 1 \\ 1 \end{bmatrix},$$

$$C(\alpha) = [\, c_1(\alpha) \quad c_2(\alpha) \quad c_3(\alpha) \quad c_4(\alpha) \quad c_5(\alpha) \,], \qquad D(\alpha) = 0$$

The interpolated linear models have the following interpretation. For any constant duty-cycle value, the static curve of Fig. 3 determines the steady-state pressure sensor voltage achieved as the dynamics approach equilibrium conditions. The interpolated linear model is intended to capture the linearized dynamics about this equilibrium condition just as the identified linear models capture the linearized dynamics about equilibrium conditions for which dynamic input-output data were collected. This clearly hinges on the assumption that the linearized dynamics vary continuously with the underlying equilibrium parameterized by the constant duty-cycle value. We see from Table 2 that certain model parameters change significant from region to region, which may ultimately impact the ability of the nonlinear model to reproduce experimental results for large amplitude duty-cycle input signals.

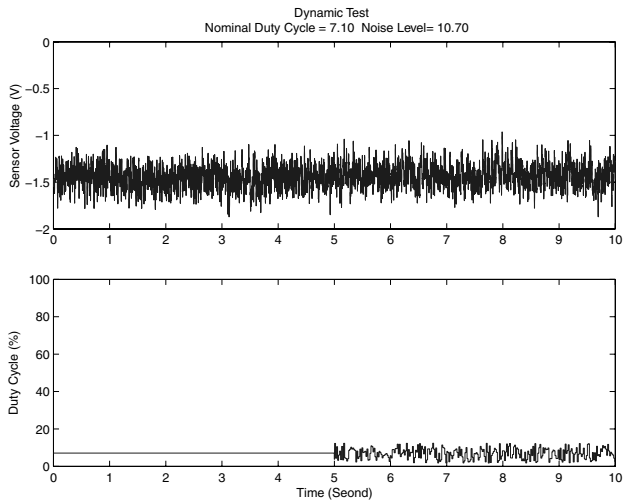

Fig. 4 Pressure sensor voltage response (top) and duty-cycle input (bottom) for Region 1 dynamic test with $u^o = 7.10\%$ and $u_\delta(t)$ amplitude = 10.70%.

D. Nonlinear Model Construction

Next, we construct a nonlinear state-space model of the form

$$\dot{x}(t) = f(x(t), u(t)) \qquad y(t) = h(x(t), u(t))$$

that satisfies the following important linearization properties with respect to the static input-output relationship derived in step 1 and the interpolated linear models constructed in step 3 based on the dynamic tests and linear system identification conducted in step 2. The first requirement imposed on the nonlinear model is that it should accurately reproduce the data represented by static curve. Specifically, for each constant duty-cycle input value $\alpha = u^o$, the nonlinear model should possess an equilibrium state x^o for which the correct constant pressure sensor voltage value $y^o = y^o(\alpha)$ is achieved. Further, it should be possible to cast the equilibrium state as a function of the constant input value as in $x^o = x^o(\alpha)$. This requirement can then be summarized mathematically by the identities

$$f(x^o(\alpha), \alpha) = 0 \qquad h(x^o(\alpha), \alpha) = y^o(\alpha)$$

The second requirement imposed on the nonlinear model is that its linearization about any equilibrium should exactly match the (interpolated) linear model for that equilibrium. This ensures that the small-signal behavior of the nonlinear model about any equilibrium is governed by the associated linear model. Writing the nonlinear model's linearization about an equilibrium corresponding to a constant duty-cycle input value $\alpha = u^o$ as

Table 3 Linear state-space model parameters

α	7.1000	26.9000	45.6000	57.7000	69.7000	87.8000
u^o	7.1000	26.9000	45.6000	57.7000	69.7000	87.8000
y^o	−1.4378	−0.9643	−0.6811	−0.6574	−0.6343	−0.5721
a_{11}	−48.6883	−16.0479	−12.9295	−18.6572	−33.7674	−118.2982
a_{21}	−378.1379	−321.8919	−334.5500	−340.4312	−387.1024	−383.9970
a_{33}	−21.9445	−22.9009	−29.4438	−40.4497	−32.5955	−26.4358
a_{43}	−112.4470	−92.5489	−108.3025	−108.5993	−126.4920	−82.9712
a_{55}	−21.3993	−22.3954	−50.0444	−37.8675	−15.0779	−127.6810
c_1	−0.0120	−0.0482	0.0375	−0.0911	−0.0177	−0.0001
c_2	0.0815	0.0119	0.0311	0.0205	−0.0185	−0.0034
c_3	0.5673	−0.1450	0.0392	−0.2817	−0.0413	−0.0020
c_4	−0.2784	0.0499	−0.0286	0.0905	0.1378	0.0404
c_5	−0.1051	−0.0191	−0.0288	−0.1565	−0.0778	−0.0420

$$\dot{x}_\delta(t) = \frac{\partial f}{\partial x}(x^o(\alpha),\alpha)x_\delta(t) + \frac{\partial f}{\partial u}(x^o(\alpha),\alpha)u_\delta(t)$$
$$y_\delta(t) = \frac{\partial h}{\partial x}(x^o(\alpha),\alpha)x_\delta(t) + \frac{\partial h}{\partial u}(x^o(\alpha),\alpha)u_\delta(t)$$

it is clear that the second requirement is equivalent to the following identities:

$$\frac{\partial f}{\partial x}(x^o(\alpha),\alpha) = A(\alpha) \qquad \frac{\partial f}{\partial u}(x^o(\alpha),\alpha) = B(\alpha)$$
$$\frac{\partial h}{\partial x}(x^o(\alpha),\alpha) = C(\alpha) \qquad \frac{\partial h}{\partial u}(x^o(\alpha),\alpha) = D(\alpha)$$

Nontrivial existence conditions must be satisfied in order for these requirements to be met. Here we proceed directly to the specification of a nonlinear model with the requisite properties. First, we point out that because the modeling objective is to predict input-output behavior from jet duty cycle to pressure sensor voltage, and because the underlying model state has no physical significance, a coordinate transformation on the model state does not interfere with the ultimate modeling goal. In the present context, consider an alternate interpolated linear model specified by

$$\hat{A}(\alpha) = A(\alpha), \qquad \hat{B}(\alpha) = A(\alpha)B(\alpha), \qquad \hat{C}(\alpha) = C(\alpha)A^{-1}(\alpha),$$
$$\hat{D}(\alpha) = D(\alpha)$$

The associated transfer function of the transformed model matches that of the original interpolated linear model as can be readily verified:

$$\begin{aligned}\hat{H}(s,\alpha) &= \hat{C}(\alpha)[sI - \hat{A}(\alpha)]^{-1}\hat{B}(\alpha) + \hat{D}(\alpha)\\ &= C(\alpha)A^{-1}(\alpha)[sI - A(\alpha)]^{-1}A(\alpha)B(\alpha) + D(\alpha)\\ &= C(\alpha)[A^{-1}(\alpha)(sI - A(\alpha))A(\alpha)]^{-1}B(\alpha) + D(\alpha)\\ &= C(\alpha)[sI - A(\alpha)]^{-1}B(\alpha) + D(\alpha)\\ &= H(s,\alpha)\end{aligned}$$

Next, consider the nonlinear model specified by the following functions:

$$f(x,u) = A(\alpha)[x + Bu]$$
$$h(x,u) = C(\alpha)A^{-1}(\alpha)[x + B\alpha] + y^o(\alpha)$$

in which α is produced by any function $\varphi(x,u)$ that satisfies $\varphi(x^o(\alpha),\alpha) = \alpha$, and we have explicitly incorporated the fact that $B(\alpha) = B$ constant, and $D(\alpha) = 0$. The first requirement is satisfied for the equilibrium state

$$x^\circ(\alpha) = -B\alpha = \begin{bmatrix} 0 \\ -\alpha \\ 0 \\ -\alpha \\ -\alpha \end{bmatrix}$$

from which it follows that $\varphi(x,u) = u, -x_2, -x_4, -x_5$ are valid choices for the function $\varphi(\cdot,\cdot)$.

As for the second requirement, using $x^o(\alpha) + B\alpha = 0$, we see that

$$\begin{aligned}\frac{\partial f}{\partial x}(x^o(\alpha),\alpha) &= \frac{\partial A}{\partial \alpha}(\varphi(x^o(\alpha),\alpha))\frac{\partial \varphi}{\partial x}(x^o(\alpha),\alpha)[x^o(\alpha) + B\alpha]\\ &\quad + A(\varphi(x^o(\alpha),\alpha))\\ &= A(\alpha)\\ &= \hat{A}(\alpha)\\ \frac{\partial f}{\partial u}(x^o(\alpha),\alpha) &= \frac{\partial A}{\partial \alpha}(\varphi(x^o(\alpha),\alpha))\frac{\partial \varphi}{\partial u}(x^\circ(\alpha),\alpha)[x^o(\alpha) + B\alpha]\\ &\quad + A(\varphi(x^o(\alpha),\alpha))B\\ &= A(\alpha)B\\ &= \hat{B}(\alpha)\end{aligned}$$

For the output equation, provided that the following necessary condition is satisfied by the static curve and interpolated linear models

$$\frac{\partial y^o}{\partial \alpha}(\alpha) = -C(\alpha)A^{-1}(\alpha)B(\alpha) + D(\alpha) = -C(\alpha)A^{-1}(\alpha)B$$

we have

$$\begin{aligned}\frac{\partial h}{\partial x}(x^o(\alpha),\alpha) &= \frac{\partial (CA^{-1})}{\partial \alpha}(\varphi(x^o(\alpha),\alpha))\frac{\partial \varphi}{\partial x}(x^o(\alpha),\alpha)[x^o(\alpha) + B\alpha]\\ &\quad + C(\alpha)A^{-1}(\alpha)\left[I + B\frac{\partial \varphi}{\partial x}[x^o(\alpha),\alpha]\right] + \frac{\partial y^o}{\partial \alpha}(\alpha)\frac{\partial \varphi}{\partial x}(x^o(\alpha),\alpha)\\ &= C(\alpha)A^{-1}(\alpha) + \left[C(\alpha)A^{-1}(\alpha)B + \frac{\partial y^o}{\partial \alpha}(\alpha)\right]\frac{\partial \varphi}{\partial x}(x^o(\alpha),\alpha)\\ &= \hat{C}(\alpha)\end{aligned}$$

and

$$\begin{aligned}\frac{\partial h}{\partial u}(x^o(\alpha),\alpha) &= \frac{\partial (CA^{-1})}{\partial \alpha}(\varphi(x^o(\alpha),\alpha))\frac{\partial \varphi}{\partial u}(x^o(\alpha),\alpha)[x^o(\alpha) + B\alpha]\\ &\quad + \left[C(\alpha)A^{-1}(\alpha)B + \frac{\partial y^o}{\partial \alpha}(\alpha)\right]\frac{\partial \varphi}{\partial u}(x^o(\alpha),\alpha) = 0 = D(\alpha)\\ &= \hat{D}(\alpha)\end{aligned}$$

Thus, with $\varphi(x,u) = u, -x_2, -x_4$ or $-x_5$, and $\alpha(t) = \varphi(x(t),u(t))$, the nonlinear model

$$\dot{x}(t) = A(\alpha(t))[x(t) + Bu(t)]$$
$$y(t) = C(\alpha(t))A^{-1}(\alpha(t))[x(t) + B\alpha(t)] + y^o(\alpha(t)) \quad (1)$$

satisfies both the static and dynamic linearization requirements. It is apparent that these requirements alone do not uniquely determine the nonlinear model as evidenced by the flexibility in choosing the scheduling variable $\alpha(t)$. Whereas different nonlinear models satisfying the linearization requirements will behave similarly when operated in a vicinity of an equilibrium condition, their nonlocal behavior may be significantly different for large deviations from an equilibrium condition. These issues are evaluated in the next step in the process.

IV. Delta-Wing Vortex Breakdown Location Controller Design

The closed-loop controller has a trajectory linearization-like structure. Trajectory linearization control (TLC) is a nonlinear control method based on linearization along a nominal trajectory. The structure of TLC is illustrated in Fig. 5. A TLC controller consists of two components: a pseudo inversion of the plant that generates the nominal control input (open-loop control), and a linear time-varying feedback regulator that stabilizes and decouples the tracking-error dynamics (closed-loop control). The nonlinear tracking and decoupling control by trajectory linearization can be viewed as the ideal gain-scheduling controller designed at every point on the trajectory. Therefore, the TLC provides robust stability and performance along the trajectory. TLC has been successfully applied in flight control [43–47] and mobile robot control [48].

The reactive flow-control system of delta-wing vortices is a TLC-type system. In the controller design, it was assumed that the gain-scheduling variable (such as the pressure command) changed slowly compared with the system dynamics. Based on this assumption, the pseudoinverse of the plant model was achieved by interpolating the static test results. By looking up the static test results, a nominal duty-cycle command was generated, which would put the pressure in the vicinity of the commanded pressure at the sensor location. Based on the slowly varying scheduling variable assumption, at each operation region, the dynamics were approximated by the local linear models identified from Sec. III.B. For each operating region, a linear feedback controller is designed to stabilize the operating error about the operating point, that is, drive the error to zero asymptotically. Then a nonlinear feedback stabilizer is designed by interpolating gains of these linear feedback

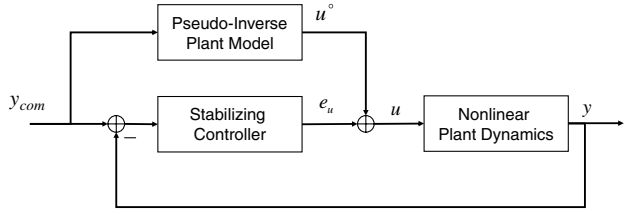

Trajectory Linearization Control

Fig. 5 Trajectory linearization control structure.

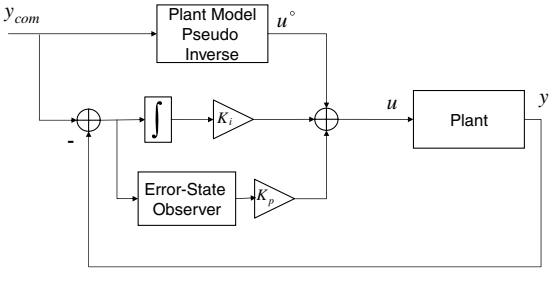

Fig. 6 Reactive flow-control system for the delta-wing vortex.

controllers using the scheduling variable. Because the error state cannot be measured directly, a gain-scheduling nonlinear error-state observer was designed to observe the error state from the output error in a manner similar to the nonlinear feedback stabilizer design. The structure of the reactive flow-control system for the delta-wing vortex is illustrated in Fig. 6.

A. Closed-Loop Controller Design

The gain-scheduled nonlinear model (1) can be rewritten as

$$\dot{x} = \hat{A}(\alpha)x + \hat{B}(\alpha)u$$
$$y = \hat{C}(\alpha)x + C(\alpha)A^{-1}(\alpha)B\alpha + y^o(\alpha) \quad \text{where } \hat{A}(\alpha) = A(\alpha), \quad (2)$$
$$\hat{B}(\alpha) = A(\alpha)B, \qquad \hat{C}(\alpha) = C(\alpha)A^{-1}(\alpha)$$

For a given command y_{com}, by looking up the static test curve, the scheduling variable and equilibrium point of the system are determined such that

$$x^o = -B\alpha \quad \text{when } u^o = \alpha \quad (3a)$$

At the equilibrium point,

$$y_{\text{com}} = y^o(\alpha) \quad (3b)$$

Assuming the scheduling variable is a constant, the system dynamics can be linearized at an equilibrium point. Define the error-state, output error, and feedback control input as

$$e_x = x - x^o(\alpha), \qquad e_y = y - y^o(\alpha), \qquad e_u = u - u^o(\alpha)$$

The error dynamics at the nominal state can be written as

$$\dot{e}_x = \hat{A}(\alpha)e_x + \hat{B}(\alpha)e_u \qquad e_y = \hat{C}(\alpha)e_x \quad (4)$$

To introduce integral output feedback to the error dynamics, we augment the error states and output as

$$\eta = \begin{bmatrix} e_x \\ \int e_y \end{bmatrix}, \qquad \zeta = \begin{bmatrix} e_y \\ \int e_y \end{bmatrix}$$

Then the augmented error dynamics are

$$\dot{\eta} = \begin{bmatrix} \hat{A}(\alpha) & \mathbf{0} \\ \hat{C}(\alpha) & 0 \end{bmatrix}\eta + \begin{bmatrix} \hat{B}(\alpha) \\ 0 \end{bmatrix}e_u \qquad \zeta = \begin{bmatrix} \hat{C}(\alpha) & 0 \\ \mathbf{0} & 1 \end{bmatrix}\eta \quad (5)$$

We design the feedback control law as

$$e_u = [\,K_p(\alpha) \quad K_i(\alpha)\,]\eta$$

Then the closed-loop system dynamics are

$$\dot{\eta} = \begin{bmatrix} \hat{A}(\alpha) + \hat{B}(\alpha)K_P(\alpha) & \hat{B}(\alpha)K_i(\alpha) \\ \hat{C}(\alpha) & 0 \end{bmatrix}\eta \quad (6)$$

If the controllability matrix of Eq. (5) has full rank, the augmented system is controllable, so we can place the closed-loop eigenvalues at any desired position.

B. Error-State Observer Design

The error-state observer is designed for the augmented error dynamics [Eq. (5)]. Suppose the observer dynamics are

$$\dot{\hat{\eta}} = \begin{bmatrix} \hat{A}(\alpha) & \mathbf{0} \\ \hat{C}(\alpha) & 0 \end{bmatrix}\hat{\eta} + \begin{bmatrix} \hat{B}(\alpha) \\ 0 \end{bmatrix}e_u \qquad \hat{\zeta} = \begin{bmatrix} \hat{C}(\alpha) & 0 \\ \mathbf{0} & 1 \end{bmatrix}\hat{\eta} \quad (7)$$

where $\hat{\eta}$ is the observer state variables, and $\hat{\zeta}$ is the observer output.

Define $\tilde{\eta} = \eta - \hat{\eta}$ and $\tilde{\xi} = \xi - \hat{\xi}$, then the error dynamics of the observer is

Table 4 Gain-scheduling feedback gains

α	7.1000	26.9000	45.6000	57.7000	69.7000	87.8000
K_p	0.5762	0.7618	0.6471	0.5845	0.5822	0.0728
	0.8711	0.7954	0.9191	0.9430	0.9285	0.9518
	−0.1775	−0.0193	−0.1020	−0.0757	−0.0983	−0.0284
	0.1831	0.0678	0.0450	−0.0021	0.0176	0.0059
	−0.7396	−0.0262	−0.0593	−0.0179	−0.0793	−0.0001
$K_i(\times 10^2)$	−32.9125	−14.0684	−51.9755	−1.8490	−3.4307	−21.0059

Table 5 Augmented error-state observer gains (observer gain is $K_o = [K_{o1} \quad K_{o2}]^T$)

α	7.1000	26.9000	45.6000	57.7000	69.7000	87.8000
K_{o1} $(\times 10^2)$	0.1122	0.1794	−0.0268	0.1228	0.1129	1.5110
	−0.1398	0.1421	−0.2568	0.0603	0.6255	3.9057
	−0.0002	0.0011	−0.0005	0.0001	−0.0009	−0.0006
	0.0002	−0.0002	0.0038	−0.0005	−0.0011	−0.0011
	0	0.0005	0.0002	0	0	−0.0003
	0	0	0	0	0	0
K_{o2}	0	0	0	0	0	0
	0	0	0	0	0	0
	0	0	0	0	0	0
	0	0	0	0	0	0
	0	0	0	0	0	0
	0.0050	0.0050	0.0050	0.0050	0.0050	0.0050

$$\dot{\tilde{\eta}} = \begin{bmatrix} \hat{A}(\alpha) & 0 \\ \hat{C}(\alpha) & 0 \end{bmatrix} \tilde{\eta} \qquad \tilde{\zeta} = \begin{bmatrix} \hat{C}(\alpha) & 0 \\ \mathbf{0} & 1 \end{bmatrix} \tilde{\eta} \tag{8}$$

By introducing a feedback law to stabilize the observer error dynamics, the error dynamics of the observer become

$$\dot{\tilde{\eta}} = \begin{bmatrix} \hat{A}(\alpha) & 0 \\ \hat{C}(\alpha) & 0 \end{bmatrix} \tilde{\eta} + K_o \tilde{\zeta} \qquad \tilde{\zeta} = \begin{bmatrix} \hat{C}(\alpha) & 0 \\ 0 & 1 \end{bmatrix} \tilde{\eta} \tag{9}$$

The system (5) is observable, and so the augmented system is also observable. We can design the observer gain to put the eigenvalues of the closed-loop observer dynamics in the desired locations.

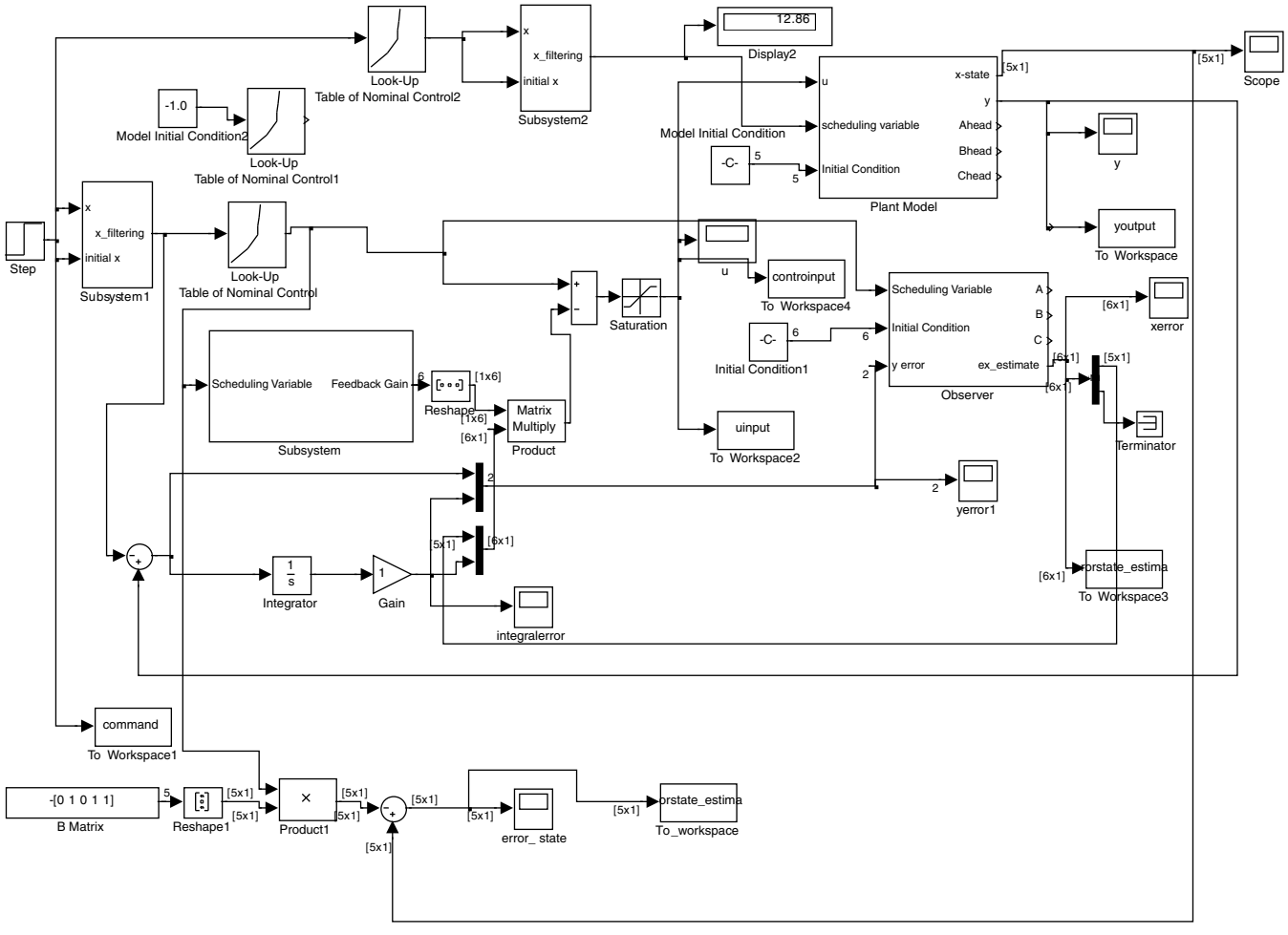

Fig. 7 Closed-loop control simulation with augmented error-state observer.

The total control input (duty cycle) is

$$u = u^o(\alpha) + [\, K_p(\alpha) \quad K_i(\alpha)\,]\hat{\eta}$$

V. Delta-Wing Vortex Breakdown Location Control Simulation and Real-Time Wind-Tunnel Test

The closed-loop vortex breakdown controller was simulated in Simulink first, and then tested in real-time wind-tunnel experiments. In the controller and observer design, the observer eigenvalues were set having a bandwidth at least three times larger than the bandwidth of the corresponding closed-loop controller eigenvalues to satisfy the singular perturbation assumption. The closed-loop controller eigenvalues were determined heuristically through tuning due to the lack of physical insight in the state variables provided by the black-box modeling approach. The feedback gains are listed in Table 4. In the controller implementation, the gain-scheduling variable is chosen as the nominal control input. The nominal control input was filtered by a low-pass filter and then fed into the gain-scheduling controller and gain-scheduling model. The observer gains are listed in Table 5.

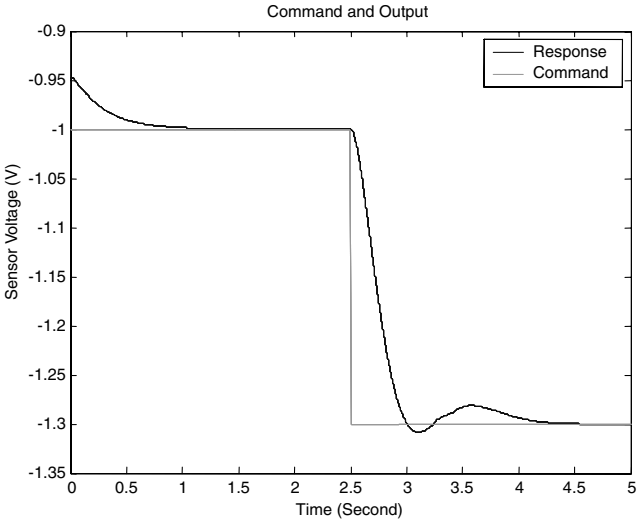

Fig. 8 Closed-loop control simulation with augmented error-state observer: command and output.

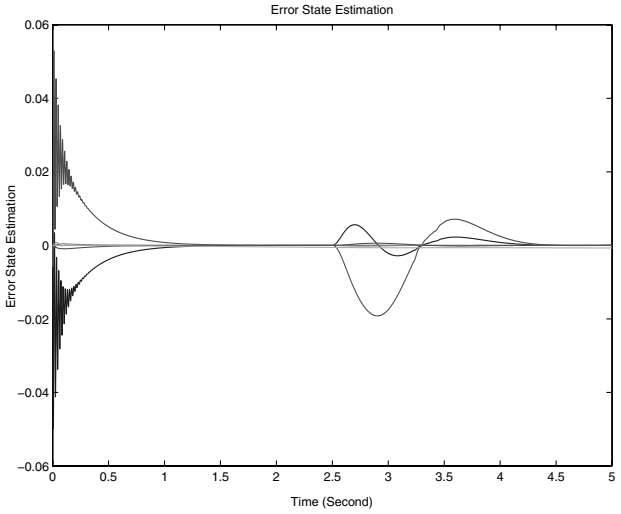

Fig. 9 Closed-loop control simulation with augmented error state observer: state-estimation error.

A. Simulation Result

Figure 7 shows the simulation diagram with augmented error-state observer. Figures 8–10 show satisfactory simulation results with the augmented observer. From Fig. 8, it can seen that the transient is smooth, and the settling time is about 1 s for the small initial error of 0.05 V at −1.0 V, and about 1.5 s for the large excursion of 0.30 V at the final value of −1.3 V. The variation of the settling time is a consequence of the nonlinear dynamics and the gain-scheduled controller. Some high-frequency damped oscillations are noticed in Fig. 9 for the observer error states in the initial 0.3 s. These oscillations could be caused by the high observer gains with large initial observer errors, which could be eliminated by further tuning. However, it appears that the controller bandwidth has eliminated these oscillations in the system response; thus, it was decided to move on to the wind-tunnel testing.

B. Real-Time Wind-Tunnel Experiment

In the real-time wind-tunnel experiment, the hardware is the Wincon/RTX system with a high-resolution PWM generator. The Simulink diagram is shown in Fig. 11. In the real-time test, the sensor output voltage was filtered by a second-order low pass in which the damping ratio is 0.707, and the bandwidth is 13 rad/s. The filtered sensor output was used as the measurement to feed into the closed-loop controller. The scheduling variable was chosen as the nominal control input. The scheduling variable and the nominal control input were smoothed by a second-order low-pass filter with damping ratio of 0.9 and a bandwidth of 6 rad/s.

In the real-time test, the controller parameters were the same as in the simulation. Before the real-time closed-loop test, a static test was conducted. In the static test, it was found that due to change in sensor calibration, there was a 0.2-V shift from the previous static data which were used in the controller design. This is almost 20% of the sensor output range. From the test result, the closed-loop controller can compensate for this shift without loss of stability. Four different commands were tested: step, pulse, sinusoidal wave, and staircase. For each test result, the command, sensor voltage output (a proxy for pressure), estimated error, and control input are shown next.

1. *Step Response*

The step command is from −0.4 to −1.3 V applied at $t = 10$ sec. Figures 12–14, show the command and the response, the state-estimation error, and the control signal, respectively. It is seen from Fig. 12 that the surface pressure tracks the step command satisfactorily, with a noticeable transport delay of about 0.2 s, a rise time (excluding the transport delay time) of about 0.2 s, a settling

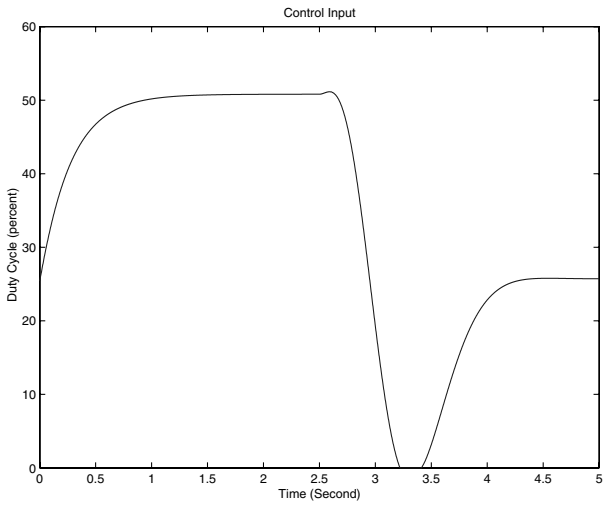

Fig. 10 Closed-loop control simulation with augmented error-state observer: control input.

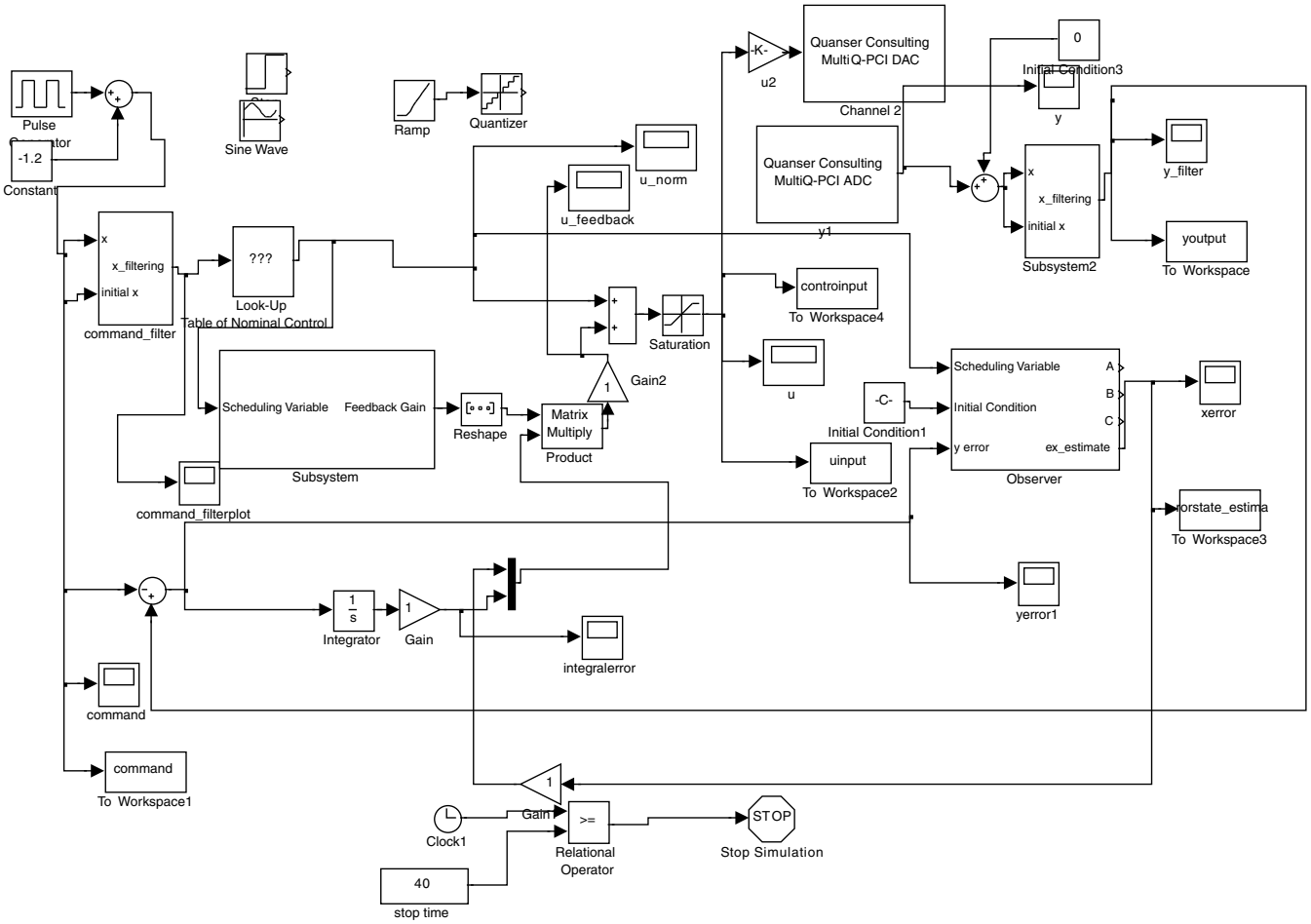

Fig. 11 Closed-loop controller real-time test Simulink diagram.

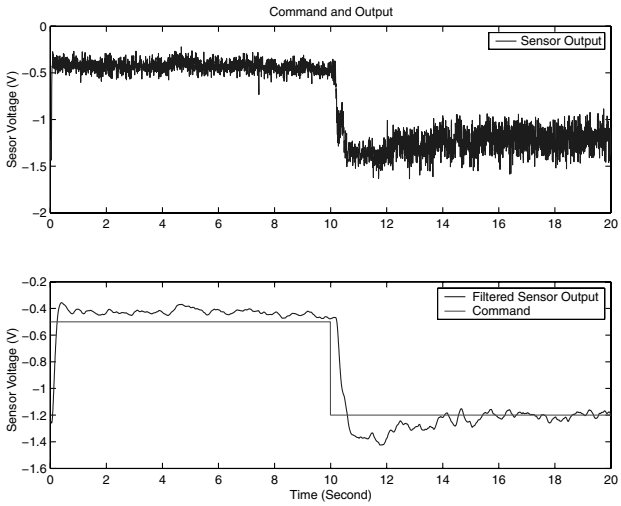

Fig. 12 Step response: command and output.

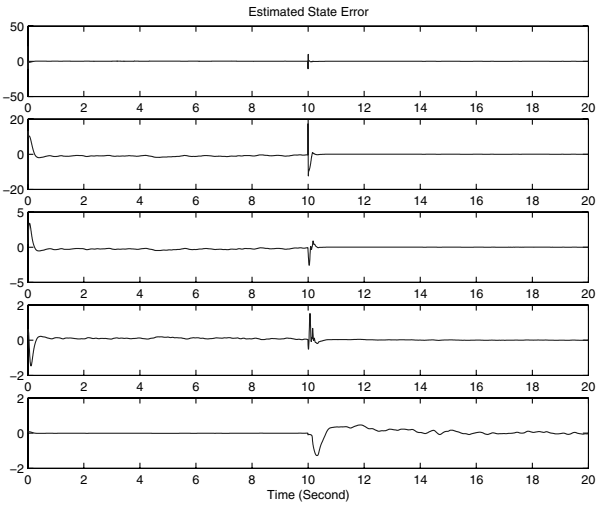

Fig. 13 Step response: state-estimation error.

time of about 3 s, and an overshoot of about 15%. It is noted that the large excursion of duty-cycle values shown in Fig. 14 before the step pressure command is applied at $t = 10$ s is due to the low control effectiveness of the PWM actuation above 40% duty cycle, in which regulating a small pressure deviation calls for large excursions of the duty cycle. It is also remarked that the tracking errors shown in Fig. 13 differ by an order of magnitude among the state variables. Because the state variables are given by the black-box model, which do not have obvious physical meaning, they are not of concern as long as the output performance is satisfactory. (The same remark applies to Figs. 16, 17, and 22 .)

2. Sinusoidal Wave Command

The command is a sinusoidal signal with a frequency of 0.5 rad/s. The amplitude of the sinusoidal signal is 0.3 V, and the bias is -1 V. Figures 15–17 show the command and the response, the state-estimation error, and the control signal, respectively.

3. Pulse Command

The command is a pulse with a 10-s period. The width of the pulse is 50%. The upper edge is -0.4 V, and the lower edge is -1.2 V.

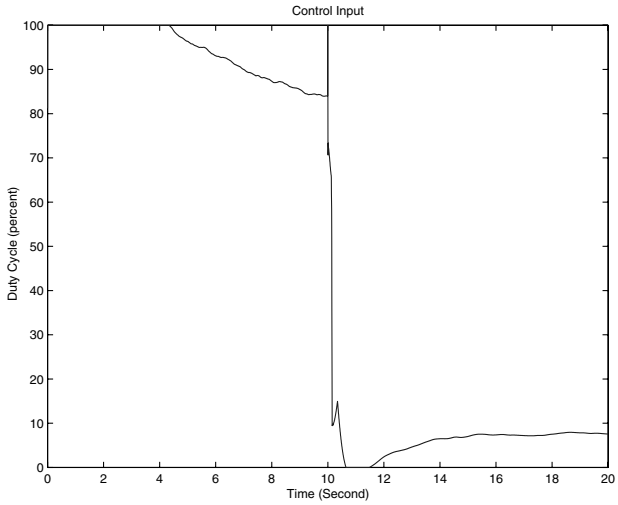

Fig. 14 Step response: control input.

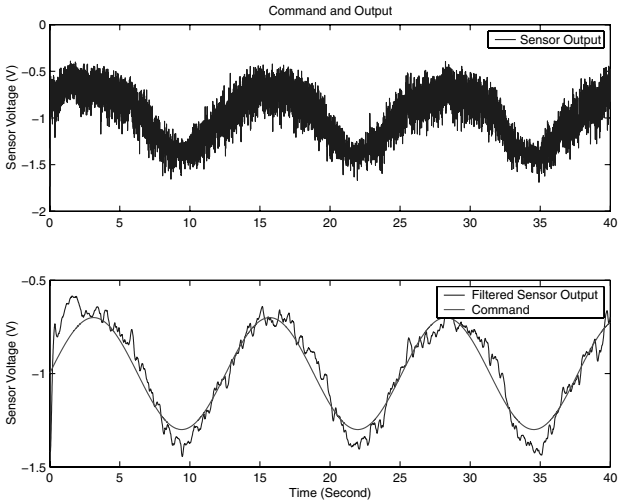

Fig. 15 Sinusoidal command: command and output.

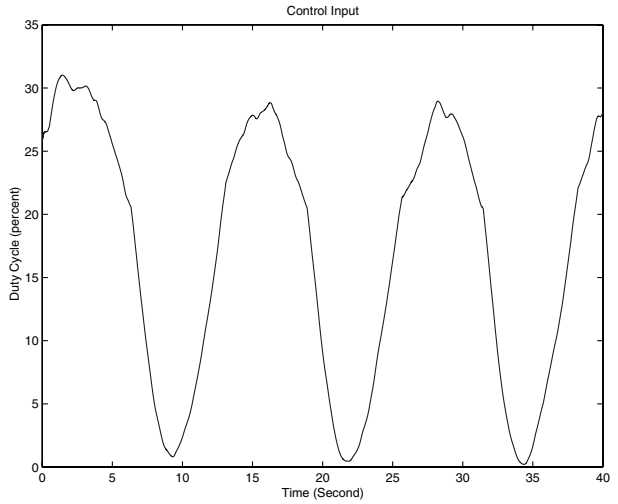

Fig. 17 Sinusoidal command: control input.

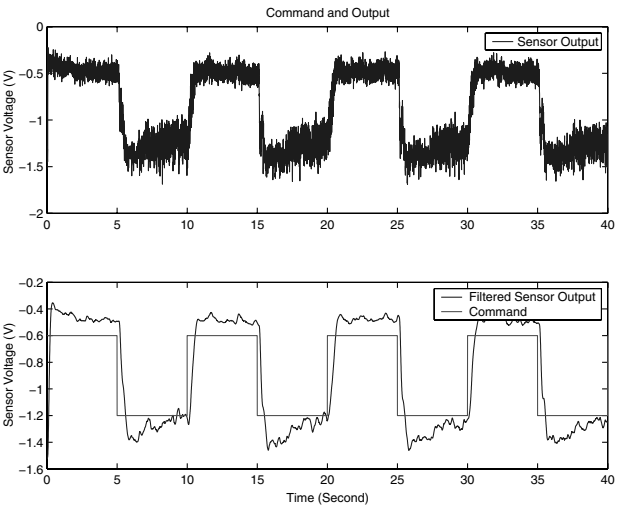

Fig. 18 Pulse response: command and output.

Figures 18–20 show the command and the response, the state-estimation error, and the control signal, respectively.

4. Staircase Response

The command is a staircase starting from −0.6 V, with step size −0.2 V. Figures 21–23 show the command and the response, the state-estimation error, and the control signal, respectively. It is seen from Fig. 21 that the surface pressure tracks the command very well up to $t = 17$ s; thereafter, it falls flat. This is caused by control saturation, as can be seen from Fig. 23, where the duty cycle reaches 0% at $t = 17$ so that the jet is completely shut off and the surface pressure can no longer be increased in magnitude.

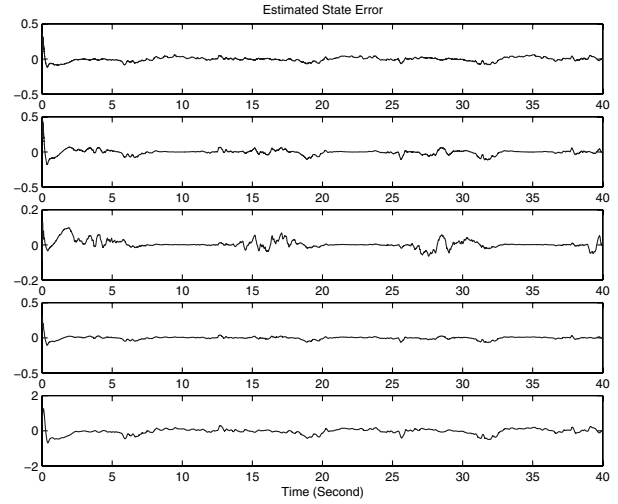

Fig. 16 Sinusoidal command: state-estimation error.

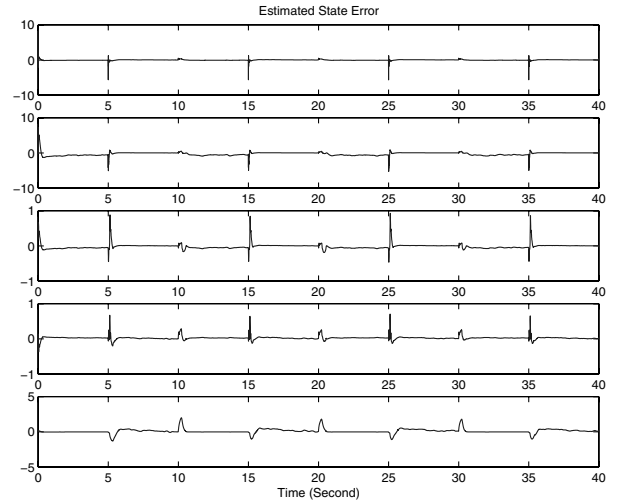

Fig. 19 Pulse response: state-estimation error.

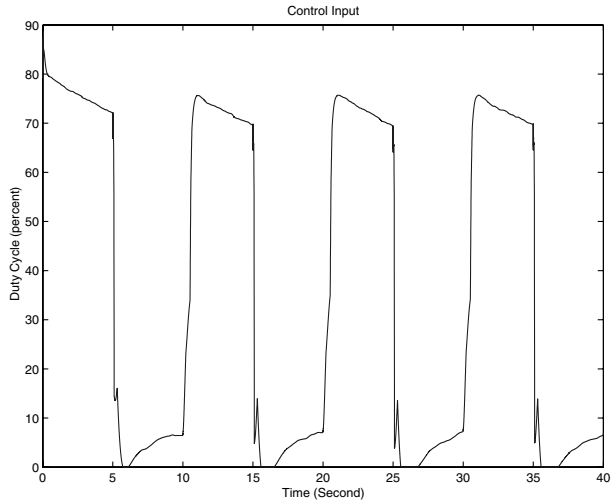

Fig. 20 Pulse response: control input.

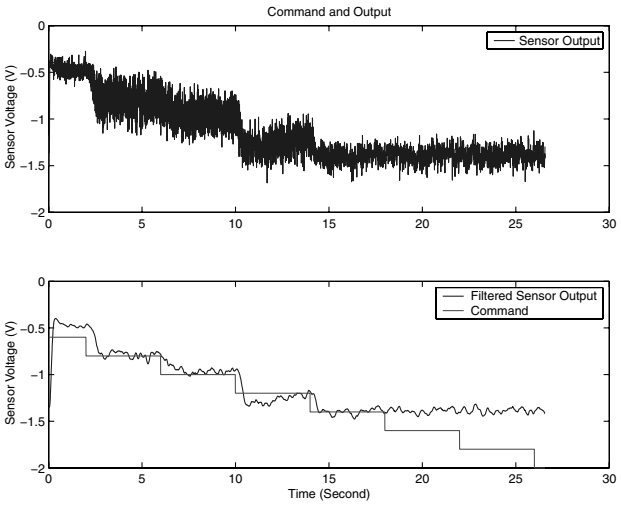

Fig. 21 Staircase response: command and response.

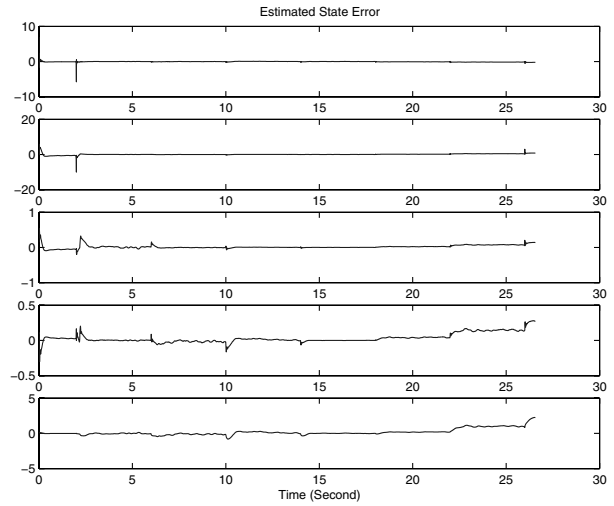

Fig. 22 Staircase response: state-estimation error.

VI. Conclusions

In this paper, the modeling and reactive flow control of delta-wing vortex breakdown location have been presented. A black-box dynamic model for active flow control of vortex breakdown location is identified using a model scheduling method [41]. Based on the identified model, a reactive flow controller is developed and real-time tested in a wind tunnel. Simulation and the real-time wind-tunnel test show that the reactive controller can effectively manipulate the upper surface pressure of the delta wing, even with perturbations induced by low turbulence levels commonly found in subsonic wind tunnels that are higher than those typical to atmospheric turbulence.

In principle, the advantages of the reactive (closed-loop active) control over open-loop active flow control include improved precision and robustness in the presence of modeling errors, dispersions in operating conditions and external disturbances, and improved transient behaviors and control energy consumption, which are critical issues for applying reactive flow control to actual aircraft. Because of limited scope and resources for the present work, a comparison study of the reactive and active control was not performed at the time of writing this paper. It is of great interest to perform such a comparative study in the future to quantify the advantages of reactive control.

The relationship between individual surface pressures and aerodynamic forces and moments necessary for flight control design was not explored. In future work, a high-bandwidth force and moment balance will be used to directly measure forces and moments generated by reactive vortex breakdown location control. A flying delta-wing aircraft using reactive flow control will be developed and tested in the future.

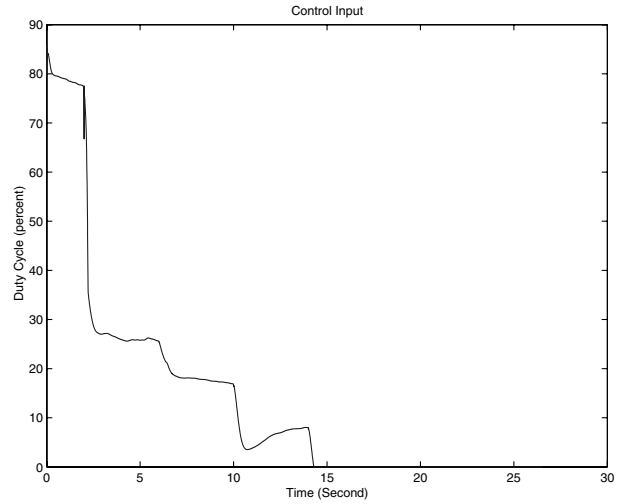

Fig. 23 Staircase response: control input.

Acknowledgment

The authors gratefully acknowledge the financial support provided by the Ohio Dayton Area Graduate Studies Institute (DAGSI).

References

[1] Mitchell, A. M., and Délery, J., "Research into Vortex Breakdown Control," *Progress in Aerospace Sciences*, Vol. 37, No. 4, May 2001, pp. 385–418. doi:10.1016/S0376-0421(01)00010-0

[2] Gursul, I., Yang, H., and Deng, Q., "Control of Vortex Breakdown with Leading-Edge Devices," AIAA Paper 95-0676, Jan. 1995.

[3] Campbell, J. F., "Augmentation of Vortex Lift by Spanwise Blowing," *Journal of Aircraft*, Vol. 14, No. 9, Sept. 1976, pp. 727–732.

[4] Dixon, C. J., "The Mechanism of Vortex Control by Spanwise Blowing and Wing Geometry," Marietta GA, Lockheed-Georgia Co., Engineering Rept. LG 78-ER-0187, June 1978.

[5] Seginer, A., and Salomon, M., "Performance Augmentation of a 60-Degree Delta Aircraft Configuration by Spanwise Blowing," *Journal of Aircraft*, Vol. 23, No. 11, 1986, pp. 801–807.

[6] Wood, N. J., and Roberts, L., "Control of Vortical Lift on Delta Wings by Tangential Leading-Edge Blowing," *Journal of Aircraft*, Vol. 25, No. 3, 1988, pp. 236–242.

[7] Maines, B. H., Moeller, B., and Rediniotis, O. K., "The Effects of

Leading Edge Suction on Delta Wing Vortex Breakdown," AIAA Paper 99-0128, Jan. 1999.
[8] Watry, C., and Helin, H., "Effects of Trailing Edge Jet Entrainment on Delta Wing Vortices," AIAA Paper 94-0072, Jan. 1994.
[9] Shih, C., and Ding, Z., "Trailing-Edge Jet Control of Leading-Edge Vortices of a Delta Wing," *AIAA Journal*, Vol. 34, No. 7, 1996, pp. 1447–1457.
[10] Vorobieff, P. V., and Rockwell, D. O., "Vortex Breakdown on Pitching Delta Wing: Control by Intermittent Trailing-Edge Blowing," *AIAA Journal*, Vol. 36, No. 4, 1998, pp. 585–589.
[11] Kuo, C. H., Lu, N. Y., and Lin, D. C., "Evolution of Vortical Structure over Delta-Wing with Transient Along-Core Blowing," *AIAA Journal*, Vol. 35, No. 4, 1997, pp. 617–624.
[12] Johari, H., and Moreira, J., "Delta Wing Vortex Manipulation Using Pulsed and Steady Blowing During Ramp-Pitching," *Journal of Aircraft*, Vol. 33, No. 2, 1996, pp. 452–453.
[13] Johari, H., Olinger, D. J., and Fitzpatrick, K. C., "Delta Wing Vortex Control via Recessed Angled Spanwise Blowing," *Journal of Aircraft*, Vol. 32, No. 4, 1995, pp. 804–810.
[14] Mitchell, A. M., Molton, P., Barberis, D., and Gobert, J. L., "Control of Vortex Breakdown by Along-the-Core Blowing," AIAA Paper 2000-2608, 2000.
[15] Gutmark, E., and Guillot, S., "Control of Vortex Breakdown over Highly Swept Wings," *AIAA Journal*, Vol. 43, No. 9, Sept. 2005, pp. 2065–2069. doi:10.2514/1.11326
[16] Amitay, M., Washburn, A. E., Anders, S. G., Parekh, D. E., and Glezer, A., "Active Flow Control on the Stingray UAV: Transient Behavior," AIAA Paper 2003-4001, June 2003.
[17] Amitay, M., Washburn, A. E., Anders, S. G., and Parekh, D. E., "Active Flow Control on the Stingray Uninhabited Air Vehicle: Transient Behavior," *AIAA Journal*, Vol. 42, No. 11, Nov. 2004, pp. 2205–2215. doi:10.2514/1.5697
[18] Washburn, A., Amitay, M., "Active Flow Control on the Stingray UAV: Physical Mechanisms," AIAA Paper 2004-0745, 2004.
[19] Malcolm, G. N., and Skow, A. M., "Flow Visualization Study of Vortex Manipulation on Fighter Configurations at High Angles of Attack," AGARD CP-413, Oct. 1986.
[20] May, C., and Gutmark, E. J., "High angle of attack flight control of delta wings using vortex actuators," AIAA Paper 2005-1232, 2005.
[21] Atwell, J. A., "Proper Orthogonal Decomposition for Reduced Order Control of Partial Differential Equations," Ph.D. Dissertation, Virginia Polytechnic Institute and State University, 2000.
[22] Ravindran, S. S., ''Proper Orthogonal Decomposition in Optimal Control of Fluids,'' NASA TM-1999-209113, 1999.
[23] Caraballo, E., Yuan, X., Little, J., Debiaso, M., Yan, P., Serrani, A., Myatt, J., and Samimy, M., "Feedback Control of Cavity Flow using Experimental Based Reduced Order Model," AIAA Paper 2005-5269, 2005.
[24] Gillies, E. A., "Low-Dimensional Control of the Circular Cylinder Wake," *Journal of Fluid Mechanics*, Vol. 371, 1998, pp. 157–178. doi:10.1017/S0022112098002122
[25] Ausseur, J., and Pinier, J., "Towards Closed-Loop Feedback Control of the Flow over NACA-4412 Airfoil," AIAA Paper 2005-343, 2005.
[26] Graham, W. R., Peraire, J., and Tang, K. Y., "Optimal Control of Vortex Shedding using Low Order Models. Part I: Open-Loop Model Development," *International Journal for Numerical Methods in Engineering*, Vol. 44, No. 7, 1999, pp. 945–972. doi:10.1002/(SICI)1097-0207(19990310)44:7<945::AID-NME537>3.0.CO;2-F
[27] Graham, W. R., Peraire, J., and Tang, K. Y., "Optimal Control of Vortex Shedding using Low Order Models. Part II: Model-Based Control," *International Journal for Numerical Methods in Engineering*, Vol. 44, No. 7, 1999, pp. 973–990. doi:10.1002/(SICI)1097-0207(19990310)44:7<973::AID-NME538>3.0.CO;2-F
[28] Rowley, C. W., "Modeling, Simulation, and Control of Cavity Flow Oscillations," Ph.D. Thesis, California Institute of Technology, 2002.
[29] Sirovich, L., "Turbulence and the Dynamics of Coherent Structures. Part I: Coherent Structures," *Quarterly of Applied Mathematics*, Vol. 45, No. 3, 1987, pp. 561–571.
[30] Gursul, I., Srinivas, S., and Batta, G., "Active control of vortex breakdown over a delta wing," *AIAA Journal*, Vol. 33, No. 9, 1995, pp. 1743–1745.
[31] Gursul, I., and Yang, H., "On Fluctuations of Vortex Breakdown Location," *Physics of Fluids*, Vol. 7, No. 1, 1995, pp. 229–231. doi:10.1063/1.868724
[32] Catafesta, L., Garg, S., Choudhari, M., and Li, F., "Active Control of Flow-Induced Cavity Resonance," AIAA Paper 1997-1804, 1997.
[33] Goman, M., and Khrabov, A., "State Space Representation of Aerodynamic Characterstics of an Aircraft at High Angles of Attack," *Journal of Aircraft*, Vol. 31, No. 5, Sep.–Oct. 1994.
[34] Huang, X. Z., and Hanff, E. S., "Prediction of Normal Force on a Delta Wing Rolling at High Incidence," AIAA Paper 1993-3686, August 1993.
[35] Murphy, P. C., and Klein, V., "Estimation of Aircraft Unsteady Aerodynamic Parameters from Dynamic Wind Tunnel Testing," AIAA Paper 2001-4016, August 2001.
[36] Juang, J.-N., and Pappa, R. S., "An Eigensystem Realization Algorithm for Modal Parameter Identification and Model Reduction," *Journal of Guidance, Control, and Dynamics*, Vol. 8, No. 5, May 1985, pp. 620–627.
[37] Moonen, M., De Moor, B., Vanderberghe, L., and Vandewalle, J., "On and Off-line Identification of Linear State Space Models," *International Journal of Control*, Vol. 49, No. 1, 1989, pp. 219–232. doi:10.1080/00207178908961241
[38] Moonen, M., and Ramos, J., "A Subspace Algorithm for Balanced State Space System Identification," *IEEE Transactions on Automatic Control*, Vol. 38, No. 11, 1993, pp. 1727–1729. doi:10.1109/9.262050
[39] Favoreel, W., De Moor, B., Van Overschee, P., "Subspace Identification of Bilinear Systems Subject to White Noise Inputs," *IEEE Transactions on Automatic Control*, Vol. 44, No. 6, 1999, pp. 1157–1165. doi:10.1109/9.769370
[40] Lawrence, D. A., and Rugh, W. J., "Gain Scheduling Dynamic Linear Controllers for a Nonlinear Plant," *Automatica*, Vol. 31, No. 3, Mar. 1995, pp. 381–390. doi:10.1016/0005-1098(94)00113-W
[41] Allwine, D. A., Strahler, J. A., Lawrence, D. A., Jenkins, J. E., and Myatt, J. H., "Nonlinear Modeling of Unsteady Aerodynamics at High Angle of Attack," AIAA Paper 2004-5275, Aug. 2004.
[42] Phillips, C. L., and Nagle, H. T., *Digital Control System Analysis and Design*, 2nd ed., Prentice–Hall, Englewood Cliffs, NJ, 1992.
[43] Bevacqua, T., Best, E., Huizenga, A., Cooper, D., and Zhu, J. J., "Improved Trajectory Linearization Flight Controller for Reusable Launch Vehicles," *42nd Aerospace Sciences Meeting, Reno, NV*, AIAA Paper 2004-0875, Jan. 2004.
[44] Mickle, M. C., and Zhu, J. J., "Bank-to-Turn Roll-Yaw-Pitch Autopilot Design Using Dynamic Nonlinear Inversion and PD-Eigenvalue Assignment," *Proceedings of the American Control Conference, Chicago, IL*, Vol. 2, IEEE, Piscataway, NJ, June 2000, pp. 1359–1364. doi:10.1109/ACC.2000.876723.
[45] Wu, X., Liu, Y., and Zhu, J. J., "Design and Real Time Testing of a Trajectory Linearization Flight Controller for the 'Quanser UFO,'" *Proceedings of the American Control Conference, Denver, CO*, Vol. 5, June 2003, pp. 3913–3918.
[46] Zhu, J. J., and Huizenga, A. B., "A Type Two Trajectory Linearization Controller for a Reusable Launch Vehicle–A Singular Perturbation Approach," AIAA Paper 2004-5184, Aug. 2004.
[47] Zhu, J., Hodel, A. S., Funston, K., and Hall, C. E., "X-33 Entry Flight Controller Design by Trajectory Linearization–A Singular Perturbational Approach," AAS Paper 01-012, Jan. 2001; also in Guidance and Control 2001, Advances in the Astronautical Sciences, Vol. 107, American Astronautical Society, pp. 151–170.
[48] Liu, Y., Zhu, J., Williams, R. L., and Wu, J., "Omni-Directional Mobile Robot Controller Based on Trajectory Linearization," *Robotics and Autonomous Systems* (accepted).